Improved Three-Dimensional CCS Method Analysis for the Reconstruction of the Peripheral Magnetic Field Structure in a Finite Beta Helical Plasma

Masafumi ITAGAKI, Kenzo ISHIMARU, Yutaka MATSUMOTO,
Kiyomasa WATANABE[1], Ryosuke SEKI[1] and Yasuhiro SUZUKI[1]

Graduate School of Engineering, Hokkaido University, Sapporo, Hokkaido 060-8628, Japan
[1]*National Institute for Fusion Science, Toki, Gifu 509-5292, Japan*

In the previous 3D Cauchy-condition surface (CCS) method analysis to reconstruct the magnetic field profile in the Large Helical Device (LHD), one assumed an impractically large number of magnetic sensors, i.e., 440 field sensors and 126 flux loops. In the singular value decomposition (SVD) process employed in the CCS method, a gap is found in the magnitude of the singular values. The most accurate field results can be obtained if all the singular values smaller than the gap threshold are eliminated, independent of the number of boundary elements on the CCS and the number of sensors as well. With the reduction in the number of boundary elements, the required numbers of field sensors and flux loops are significantly reduced to 110 and 25, respectively, without losing the solution accuracy. They can be further reduced to 58 and 13 respectively if considering the symmetry of the field profile in the LHD. This result suggests the possibility of actual application to the LHD.

1. Introduction

In a nuclear fusion device, the plasma boundary shape is one of the important parameters to identify the MHD equilibrium configuration. There have been several approaches to identifying the boundary shape independently of the pressure and the current profile, deduced from signals of magnetic sensors located outside the plasma. One such method [1, 2] uses a small number of current 'filaments' assumed at fixed positions within the plasma. The currents in these filaments are then computed in such a way that one obtains the best fit to the measured magnetic fluxes and fields. In contrast, J. Svensson and A. Werner [3] assumed a large number of filaments (beams) and inferred the distribution of possible flux surface topologies with the use of a Bayesian approach. Instead of such filaments, Feneberg *et al.* [4] assumed a 'control surface' inside the plasma. The current density distribution on the surface is expressed as a sum of Fourier modes. Hofmann and Tonetti [5] proposed a method based on finite element basis functions to represent the plasma current distribution. Kurihara [6] proposed the Cauchy condition surface (CCS) method, which has been established for real-time operating control and diagnosis of JT-60U [6, 7], a tokamak. Here, the Cauchy condition surface (CCS), where both the Dirichlet and the Neumann conditions are unknown, is hypothetically placed in a domain that can be supposed to

be inside the plasma. In the analysis, no plasma current is assumed outside this CCS, where in reality the plasma current does exist.

The works mentioned above focus mainly on tokamaks, i.e., axisymmetric plasmas, so that the analyses can be made in a 2-dimensional (2D), *r-z* system. On the other hand, 3D analyses are required for non-axisymmtric plasmas, e.g., in a helical type device such as the Large Helical Device (LHD) of the National Institute for Fusion Science (NIFS). In the LHD, it is important to consider the following characteristics of the plasma current:

(i) The plasma current itself is much weaker than the toroidal current in a tokamak device.
(ii) The dominant plasma current is the so-called Pfirsch-Schülter current, the average of which over a magnetic surface is zero. However, this current still has a 3D profile.

It is therefore difficult to apply most of the simplified methods quoted above to the plasma in a helical-device. Among them, however, the CCS method [6] has a rigorous mathematical background (see the Appendix of Ref. [8]) that is applicable to 3D problems.

Recently, the authors' research group developed the 3D Cauchy condition surface method [8, 9] to reconstruct the 3D magnetic field profile outside the non-axisymmetric plasma in the LHD. This 3D CCS method is not a straight-

author's e-mail: itagaki@qe.eng.hokudai.ac.jp

forward extension of Kurihara's 2D CCS method. The magnetic flux function ψ that satisfies the Grad-Shafranov equation is at the same time a surface function that satisfies $\boldsymbol{B} \cdot \nabla \psi = 0$. The plasma boundary in an axisymmetric plasma can then be easily identified by drawing contours of the scalar function ψ. Unfortunately, however, it is not easy to define such a surface function for the 3D non-axisymmetric plasma. The process of the 3D CCS analysis is a little more complicated. First, one solves the 3D Laplace equation and in this case the unknowns to be solved are vector potentials (not scalar quantities) on the CCS. Next, one reconstructs a 3D profile of magnetic field. Furthermore, one needs to perform a magnetic field line tracing to investigate the magnetic surface structure.

As the 3D analyses consume a large number of unknowns, the problem becomes very ill-conditioned. The 10-fold rotational symmetry in the toroidal direction of the LHD was considered to reduce the number of unknowns [8–10]. However, the condition number [11] of the solution matrix still exceeds 10^{15} in some cases. In the beginning of the research [8], the Tikhonov regularization technique [11] was introduced so that the condition number was reduced to about 10^7. Later, the truncated singular value decomposition (TSVD) technique [11] instead of Tikhonov's regularization technique was adopted since conveniently, the desired condition number can be specified directly in advance. In the newer analysis using the TSVD technique [9] the reduced condition number was set to be 10^5. The effect on the solution accuracy was satisfactory, however, no guideline for the best regularization in the SVD technique has not yet been well investigated at this time.

In the previous work [9], the authors' research group succesfully reconstructed the magnetic field profile in the LHD with a fairly acceptable accuracy, so that the last closed magnetic surface (LCMS) could also be identified with the aid of magnetic field line tracing for the reconstructed field. However, in this analysis they had to assume 440 field sensors and 126 flux loops. It is impractical to assume such a large number of sensors. An effort should be made to reduce the number of magnetic sensors required for the analysis.

In order to realize an inverse analysis with a smaller number of sensors, possible measures are (a) reduction in the number of unknowns, (b) consideration of the symmetry of magnetic field profile and (c) interpolation of the sensor signals. In the present research, the authors direct their attention mainly to the reduction in the number of unknowns, i.e., the number of nodal points on the CCS that is modeled by boundary elements. In more detail, it is found that by considering the behaviour of singular values in the TSVD process the magnetic field can be accurately reconstructed with a small number of boundary elements and hence with a small number of sensor signals. It is also reported that, considering the symmetry of the field profile in the LHD, the required number of magnetic sensors can

be further reduced by half.

This paper is arranged as follows. The outline of the 3D CCS method is given in Sec. 2. Section 3.1 reviews the CCS analysis previously reported in Ref. [9], which was performed using 440 field sensors and 126 flux loops. In Sec. 3.2, one shows that there is a gap in the magnitude of singular values, and finds that the most accurate field profile can be reconstructed if one filters out all the singular values smaller than the gap threshold, independent of the number of unknowns. In Sec. 3.3, an analisys is made assuming only 110 field sensors and 25 flux loops with 12 boundary elements on the CCS. This can be made by truncating the singular values smaller than the gap. In spite of the drastic reduction in the number of sensors, one can observe better accuracy of the reconstructed field than that reported in Ref. [9]. Section 3.4 describes the magnetic field line tracing for the reconstructed field distribution. Section 3.5 shows Poincaré plots for field line traces originating at various starting points. Also, using the radial basis function (RBF) expansion [12] the Poincaré plot points are converted to a 'quasi magnetic surface', which shows an acceptable agreement with the true magnetic surface. It is shown in Sec. 3.6 that the numbers of field sensors and flux loops can be further reduced to 58 and 13 respectively if one considers the symmetry of the field profile in the LHD. Concluding remarks are in Sec. 4. As the reduced number of sensors required is almost the same as the number of sensors installed in the LHD, the present research results suggest the possibility of actual application to the LHD.

2. Outline of the 3D CCS Method

The Cauchy-condition surface (CCS), where both the Dirichlet and the Neumann conditions (the vector potential $\boldsymbol{A}$ and its normal derivative $\partial \boldsymbol{A} / \partial \boldsymbol{n}$) are unknown, is hypothetically placed in a domain that can be supposed to be inside the plasma. In the analysis, no plasma current is assumed outside this CCS, where in reality plasma current does exist. Instead, the CCS plays the same role as the plasma current in causing the field outside the plasma.

In the beginning of the research [8] the authors adopted the simple 'axisymmetric CCS' shown in Fig. 1 (a) that has a circular cross section with radius 0.075 m. However, they now use the 'twisted CCS' shown in Fig. 1 (b). In this new model [9], the ellipse given by

$$\frac{(r - r_0)^2}{a^2} + \frac{(z - z_0)^2}{b^2} = 1, \qquad (1)$$

rotates 180° clockwise in the poloidal direction when it proceeds 36° counterclockwise in the toroidal direction following the variation in vacuum vessel geometry of the LHD. Independent of the toroidal angle, the twisted CCS can keep a certain distance from its surface to the LCMS. A reduction in the numerical error can then be expected.

In the present work, the values of a and b in Eq. (1) are 0.15 m and 0.375 m, respectively, i.e., the minor axis is
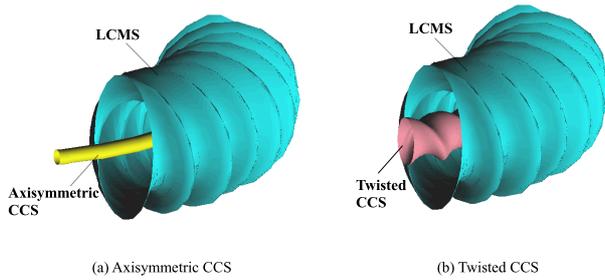
(a) Axisymmetric CCS (b) Twisted CCS

Fig. 1 Images of the axisymmetric CCS and the twisted CCS. (a) Axisymmetric CCS. (b) Twisted CCS.

30 cm and the major axis 75 cm, respectively. The center of the CCS is set to be at $r_0 = 3.7303$ m (major radius) and $z_0 = 0.0$ m.

A 3D Cartesian coordinate system is adopted to realize a boundary-only integral formulation. The first step of the analysis is to solve the following boundary integral equations (BIEs) and obtain the values of the vector potential and its derivative on the CCS in such a way that they will be consistent with the sensor signals.

(i) For magnetic field sensor locations i:

$$B_j - W_j^{(B)} = \sum_k \int_{\Gamma_{\text{CCS}}} \left\{ (L_k^j \phi_i^*) \frac{\partial A_k}{\partial n} - A_k \left(L_k^j \frac{\partial \phi_i^*}{\partial n} \right) \right\} d\Gamma.$$
$$(j = r, \varphi, z; \ k = x, y, z) \quad (2)$$

The operator L_k^j corresponds to a component in $\boldsymbol{B} = \nabla \times \boldsymbol{A}$ with $\boldsymbol{A}$ expressed in Cartesian coordinates, $W_j^{(B)}$ is the contribution of external coil currents, and ϕ_i^* the fundamental solution of the Laplace equation.

(ii) For flux loops:

e.g., the BIE for a circle loop set in the toroidal direction is given as

$$\psi^{(Tor)} - W^{(Tor)}$$
$$= \sum_k \int_{\Gamma_{\text{CCS}}} \left\{ \frac{\partial A_k}{\partial n} \left(\int_0^{2\pi} \eta_k \phi_i^* d\varphi \right) - A_k \left(\int_0^{2\pi} \eta_k \frac{\partial \phi_i^*}{\partial n} d\varphi \right) \right\} d\Gamma,$$
$$(k = x, y) \quad (3)$$

with $\eta_x = -R \sin \varphi$ and $\eta_y = R \cos \varphi$ for the radius R of the circle loop.

(iii) For points i on the CCS (Γ_{CCS}):

$$\frac{1}{2} A_{k,i} = \int_{\Gamma_{\text{CCS}}} \left(\phi_i^* \frac{\partial A_k}{\partial n} - A_k \frac{\partial \phi_i^*}{\partial n} \right) d\Gamma. \quad (k = x, y, z) \quad (4)$$

The above three types of BIEs are discretized and coupled. Further, considering the 10-fold rotational symmetry of the LHD in the toroidal direction, the number of unknowns is

reduced by a factor of 10 with the aid of a linear transformation of the vector potential expressed in the Cartesian coordinate system [8–10]. The 36° portion of the CCS torus was divided into a certain number of discontinuous quadratic boundary elements, each of which has nine nodal points [13]. Eventually the set of equations is converted to a matrix equation that has the form

$$\boldsymbol{D}\boldsymbol{p} = \boldsymbol{g}, \quad (5)$$

where the solution vector $\boldsymbol{p}$ contains the vector potentials $\boldsymbol{A} = (A_x, A_y, A_z)$ and their normal derivatives $\partial \boldsymbol{A} / \partial n$ on the CCS. This matrix equation is solved using the singular value decomposition (SVD) technique [14]. The matrix $\boldsymbol{D}$ is decomposed as $\boldsymbol{D} = \boldsymbol{U} \boldsymbol{\Lambda} \boldsymbol{V}^T$, where $\boldsymbol{U}$ and $\boldsymbol{V}^T$ are orthogonal matrices. The matrix

$$\boldsymbol{\Lambda} = \begin{bmatrix} \lambda_1 & 0 & \cdots & 0 \\ 0 & \lambda_2 & \cdots & 0 \\ \vdots & \vdots & \ddots & \vdots \\ 0 & 0 & \cdots & \lambda_n \end{bmatrix}, \quad (6)$$

is a diagonal matrix with nonnegative components, where the singular values λ_i appear in non-increasing order, $\lambda_1 \geq \lambda_2 \geq \cdots \geq \lambda_i \cdots \geq \lambda_n \geq 0$. The ratio of the largest to the smallest singular values λ_1 / λ_n is called the condition number [11]. When the condition number is very large, i.e. $\boldsymbol{\Lambda}$ includes very small singular values, it causes a numerical instability of the solution. To avoid this, the truncated SVD technique [11] was employed. The regularized solution in this case is given by

$$\boldsymbol{p} = \boldsymbol{V} \boldsymbol{\Lambda}_k^{-1} \boldsymbol{U}^T \boldsymbol{g}, \quad (7)$$

where $\boldsymbol{\Lambda}_k$ means that the singular values smaller than λ_k in $\boldsymbol{\Lambda}$ are omitted so that the reduced condition number (the ratio λ_1 / λ_k) is not larger than a certain value.

Once all the values of the conditions on the CCS are known, the magnetic fields for arbitrary points outside the CCS can be calculated using the formula

$$B_j = \sum_k \int_{\Gamma_{\text{CCS}}} \left\{ \left(L_k^j \phi_i^* \right) \frac{\partial A_k}{\partial n} - A_k \left(L_k^j \frac{\partial \phi_i^*}{\partial n} \right) \right\} d\Gamma + W_j^{(B)}.$$
$$(j = r, \varphi, z; \ k = x, y, z) \quad (8)$$

Note here that the external coil effect $W_j^{(B)}$ is added to the field caused by the plasma current. The magnetic field line tracing can be made for the field distribution computed using Eq. (8).

3. Numerical Tests for the LHD

One considers the plasma with the magnetic field strength, the magnetic axis location and the volume-averaged β being $B_{\text{ax}} = 3$ T, $R_{\text{ax}} = 3.6$ m and $\langle \beta \rangle = 2.7\%$ respectively in the LHD. The reference MHD equilibrium for this condition had been analyzed beforehand [15] using the 3D MHD equilibrium calculation code HINT2 [16].

That is, the magnetic sensor signals and the magnetic field caused by the external coil currents are known before the present analysis. The reconstructed results are compared with the reference solutions.

For the sake of the discussion from now on, the authors should give the definition of the last closed magnetic surface (LCMS). In this work, the LCMS means the outermost closed surface that is recognized through field line tracing with the Poincaré plot. If the tracing is made for the accurate magnetic field distribution that is rigorously calculated using the HINT2 code, the Poincaré plot draws the LCMS clearly and correctly. On the other hand, the field profile reconstructed using the CCS method as an inverse analysis is usually a little dirty, so that the reconstructed LCMS is not very clear but somewhat indistinct in most cases.

3.1 Use of 440 field sensors and 126 flux loops

As each boundary element on the CCS has 9 nodes, the total number of nodes is given by $N = 9n_{BE}$, where n_{BE} is the number of boundary elements. The number of unknowns is then given by $6N = 54n_{BE}$, i.e., the product of $N (= 9n_{BE})$, components of vector potential $(= 3)$ and boundary conditions at each node $(= 2$: the Dirichlet and the Neumann conditions). Since one consumes $3N$ equations for points i on the CCS (see Eq. (4)), the number of sensor signals must be larger than the remaining number of equations, i.e., $3N$.

One here uses 48 boundary elements on the CCS, so that the number of unknowns is $54n_{BE} = 2592$. Due to this, one assumes 440 magnetic field sensors. Since each of the field sensors is assumed to detect all of the three components of magnetic field, the total number of signals $(= 440 \times 3 = 1320)$ is a little larger than $3N = 1296$. In addition to the field sensors, one also assumes 126 flux loops. Consequently, the total number of sensor signals becomes 1446 $(= 1320 + 126)$, which is larger than $3N = 1296$.

Figure 2 illustrates sensor locations in the r-z plane at the toroidal angle of 18 deg (the horizontally elongated cross-section). The 440 field sensors are purposely placed on 11 different r-z planes at 3.6° intervals within the range of toroidal angle, $0° \leq \varphi \leq 36°$. This arrangement of sensors is identical to the case where all of the sensors are distributed carefully for the whole range of $0° \leq \varphi \leq 360°$ in such a way that there will be no equivalent point under the 10-fold rotational symmetry. The small circles in Fig. 2 illustrate the positions of 40 field sensors placed in this r-z plane.

The black dots in Fig. 2 show the set of 100 magnetic flux loops in the toroidal direction, each of which is at a distance of 0.9 m from the point $(r, z) = (3.7303 \, \text{m}, 0.0 \, \text{m})$. The two circles depict the flux loops in the poloidal direction, which have radii of 1.0 m and 1.2 m respectively with
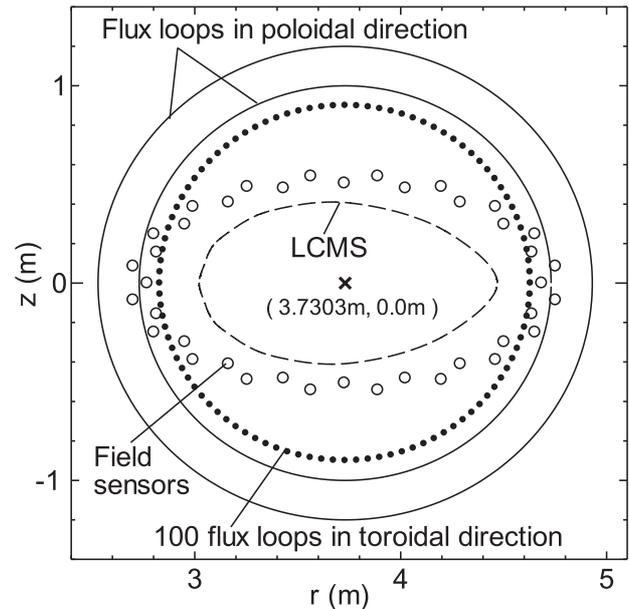

Fig. 2 Sensor locations on the horizontally elongated cross-section: 440 field sensors and 126 flux loops.

the center $(r, z) = (3.7303 \, \text{m}, 0.0 \, \text{m})$. A total of 26 flux loops of this type are set in 13 different r-z planes at 3.0° intervals within the range of $0° \leq \varphi \leq 36°$.

All of the above sensor locations are exactly the same as those used in the previous work [8, 9].

The CCS analysis is made in such a way that the sensor signals are reproduced. Figures 3 (a)-(d) depict the reproduction of field sensor signals for different values of reduced condition number when using 48 boundary elements on the CCS. In each figure, the abscissa represents the original sensor signal, whereas the ordinate indicates the value reconstructed from the CCS computation. The points denoting B_r, B_φ and B_z scatter around the diagonal line $(y = x)$ in all figures, but it is found that the larger the condition number is, the smaller the scatter is. However, good reproduction of the sensor signals does not always mean good reconstruction of the entire profile of magnetic field.

Figures 4 (a), (b) and (c) show the reconstructed field profiles (the external coil effect is not included) when the condition number is assumed to be 10^5. These figures give the contours of B_r, B_φ and B_z respectively on the horizontal elongated cross section. In each figure, the reconstructed solution is shown on the left, while the reference one is on the right-hand side. The results are exactly the same as those found in Ref. [9]. Guidelines for the best choice of the condition number have not been well investigated up to now.

3.2 Behavior of the singular values

Figures 5 (a) and (b) show the behavior of the singular values which appeared in the singular value decomposition process when assuming 440 field sensors and 126 flux
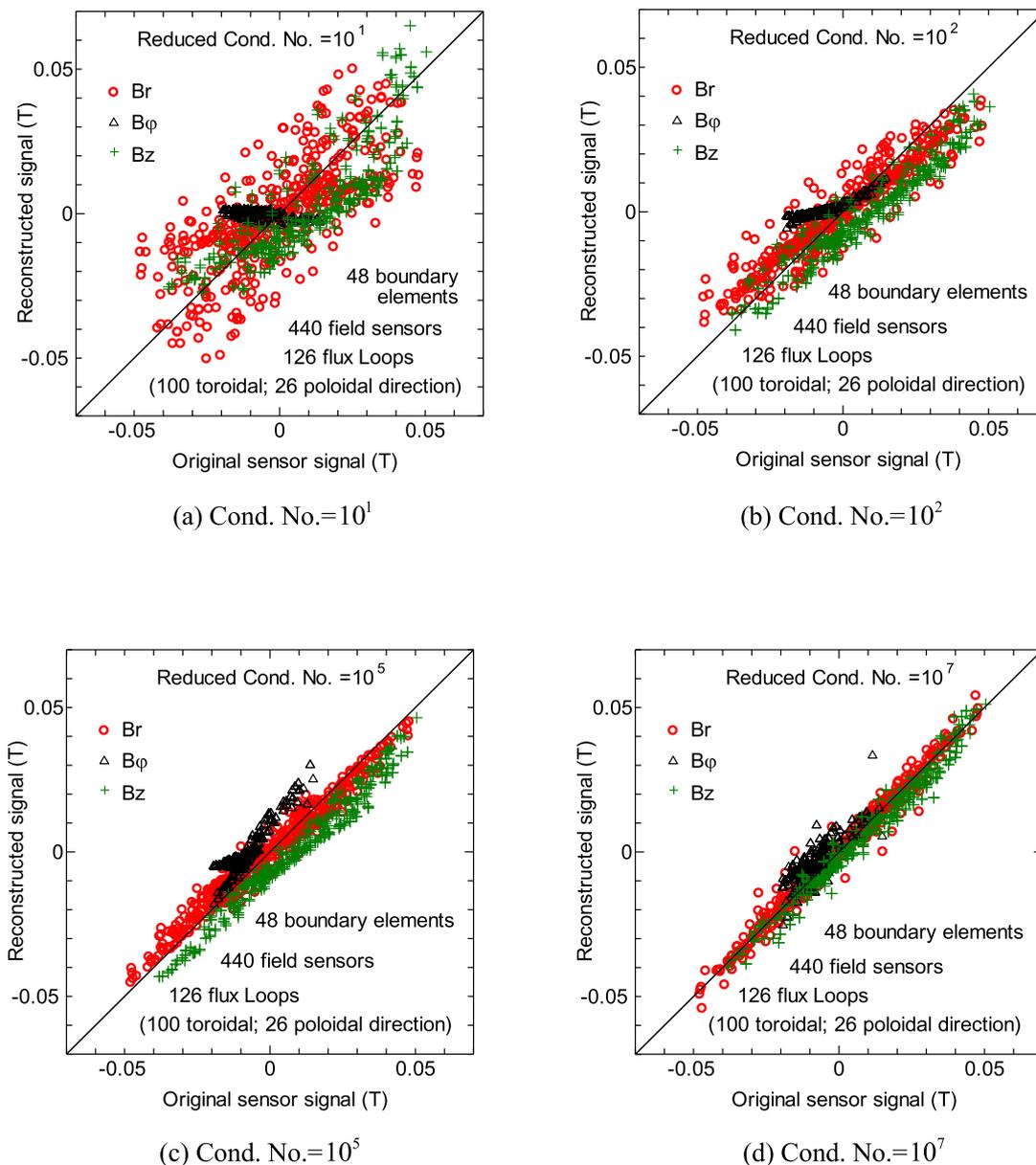
(a) Cond. No.=10^1

(b) Cond. No.=10^2

(c) Cond. No.=10^5

(d) Cond. No.=10^7

Fig. 3   Reconstructions of field sensor signals. (a) Cond. No.= 10^1. (b) Cond. No.= 10^2. (c) Cond. No.= 10^5. (d) Cond. No.= 10^7.

loops with the twisted CCS. The vertical axis in each figure represents the singular values whose maximum value is normalized to unity. In both figures, 'TnPm' means that the CCS is divided into n and m boundary elements in the toroidal direction and the poloidal direction respectively, i.e., nm is identical to n_{BE}, the number of boundary elements. In the T8P6 case, the number of unknowns is then $6N = 54\,nm = 2592$, which agrees with the number of singular values found in the SVD process.

It is observed in Fig. 5 (a) for the T8P6 case that there is a gap between 5.03×10^{-2} and 1.01×10^{-3} in the magnitude of the normalized singular values. It is interesting to point out that the numbers of singular values larger and smaller than this gap threshold around 10^{-2} are both 1296, exactly the same as each other. This phenomenon is always the case independent of the number of boundary elements.

In Fig. 5 (b) the gap threshold can be found commonly in the vicinity of 10^{-2} in the normalized singular values for all cases of the boundary element segmentations.

Hereafter one will use the term the 'reduced condition number' that is defined as the reciprocal of the normalized singular value when one cuts off the values lower than this value. It will be shown that the most accurate reconstruction can be realized if all the singular values smaller than the gap threshold are eliminated.

To evaluate the reconstructed solution accuracy, the reconstructed field results were compared with the reference solution obtained using the HINT2 code. Theoretically the field reconstructed using the CCS method under the vacuum field assumption agrees exactly with the true field if there is no plasma current. Notice that even outside the LCMS plasma currents exist to some extent, although
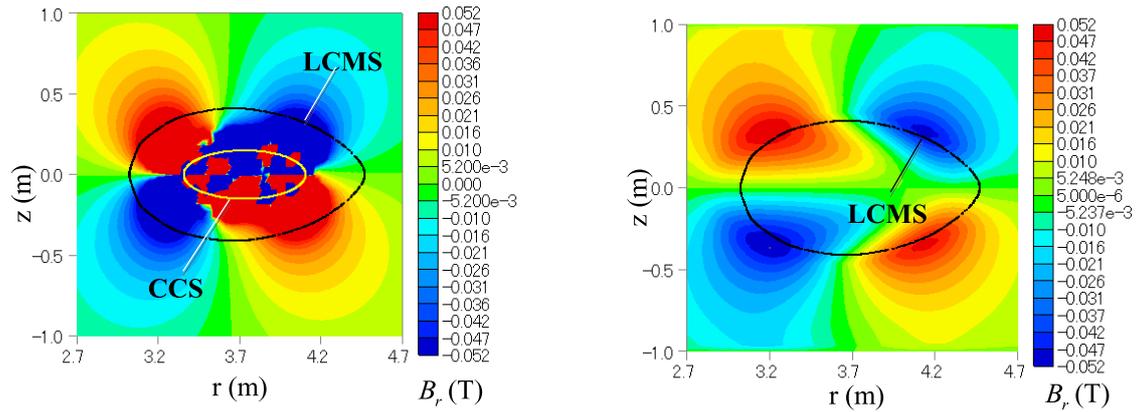
(a) B_r (Left: Reconstructed. Right: Reference.)
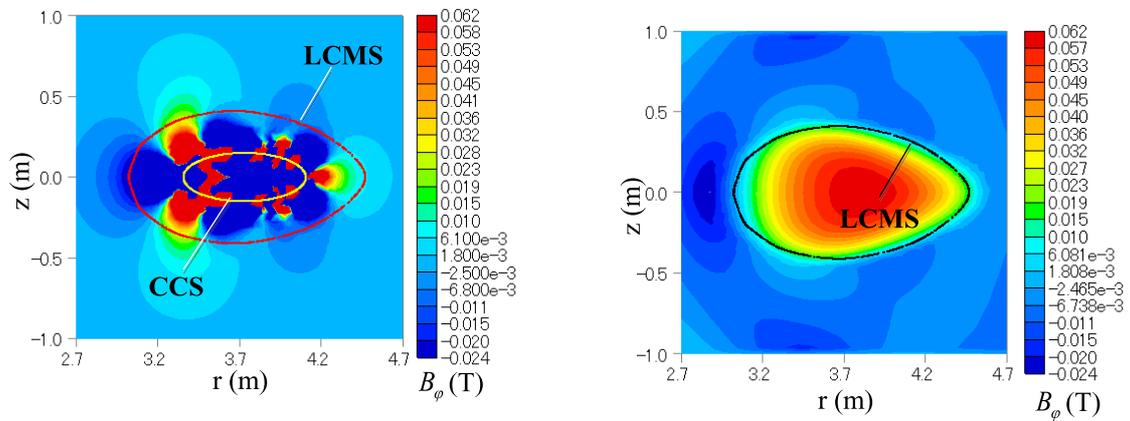
(b) B_φ (Left: Reconstructed. Right: Reference.)
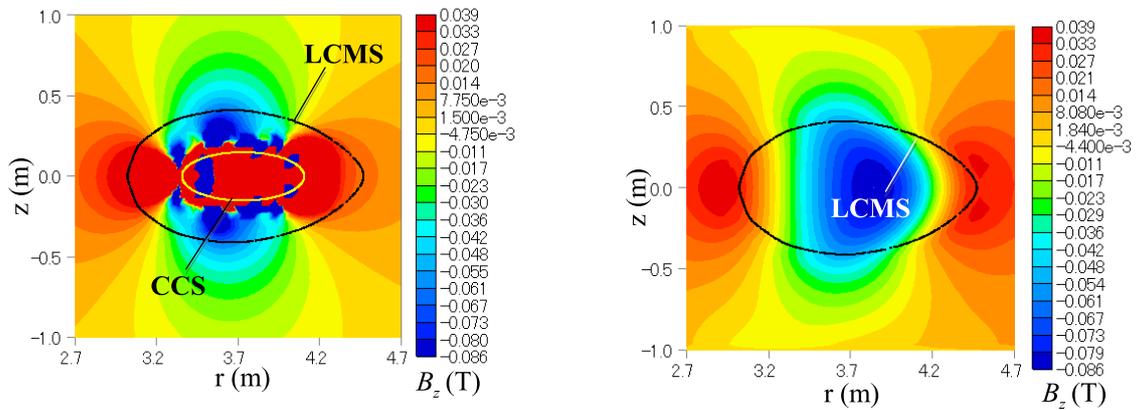
(c) B_z (Left: Reconstructed. Right: Reference.)

Fig. 4 Reconstructed field caused by plasma current only when assuming 440 field sensors and 126 flux loops with 48 boundary elements (T8P6). The condition number was set to be 10^5. (a) B_r (Left: Reconstructed. Right: Reference.). (b) B_φ (Left: Reconstructed. Right: Reference.). (c) B_z (Left: Reconstructed. Right: Reference.).

they are weak. The field errors near the LCMS are therefore the most important for the field reconstruction using the CCS method. Hereafter, based on the LCMS that is given for the reference magnetic field, all the error tendencies are investigated for the region $1.0 < \rho < 1.1$ in the minor radius (ρ) space, i.e. very near the LCMS.

Figure 6 (a) for the T8P6 case and Fig. 6 (b) for the T5P4 case show (i) the maximum errors of each component of the field and (ii) the portion of the area (%) where the error is larger than 0.02 T, as a function of the condition number after the truncation. In both cases the most accurate results can be obtained when the condition number is
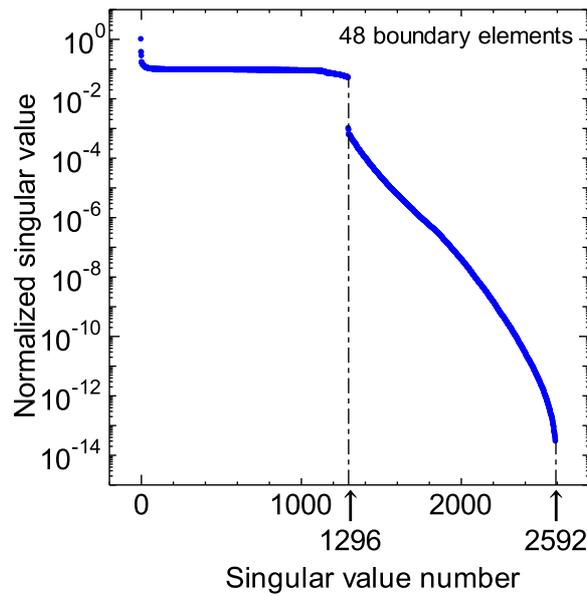
(a) Singular values for the T8P6 case
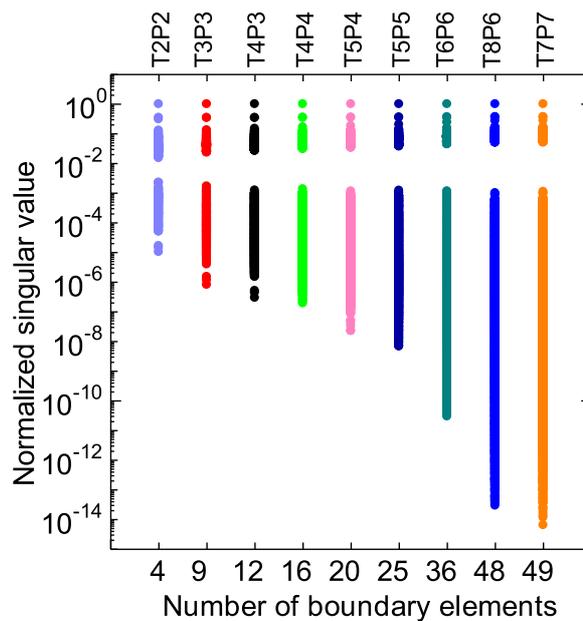
(b) Singular values as a function of the number of boundary elements
when using 440 field sensors and 126 flux loops

Fig. 5   Behavior of singular values. (a) Singular values for the T8P6 case. (b) Singular values as a function of the number of boundary elements when using 440 field sensors and 126 flux loops.

almost 10^2, i.e., when all the singular values smaller than the gap threshold are filtered out.

3.3   Reduction in the number of magnetic sensors

In this section one will perform an analysis with only 110 field sensors and 25 flux loops set in the toroidal di-

rection, as shown in Fig. 7. In this occasion, one does not adopt any flux loop set in the poloidal direction since it has been found that its signal is less sensitive to the magnetic field reconstruction than that of the loop set in the toroidal direction. The number of sensors cannot be reduced effectively without reducing the number of unknowns, i.e., the number of boundary elements on the CCS. Following

(a) 48 boundary elements (T8P6)
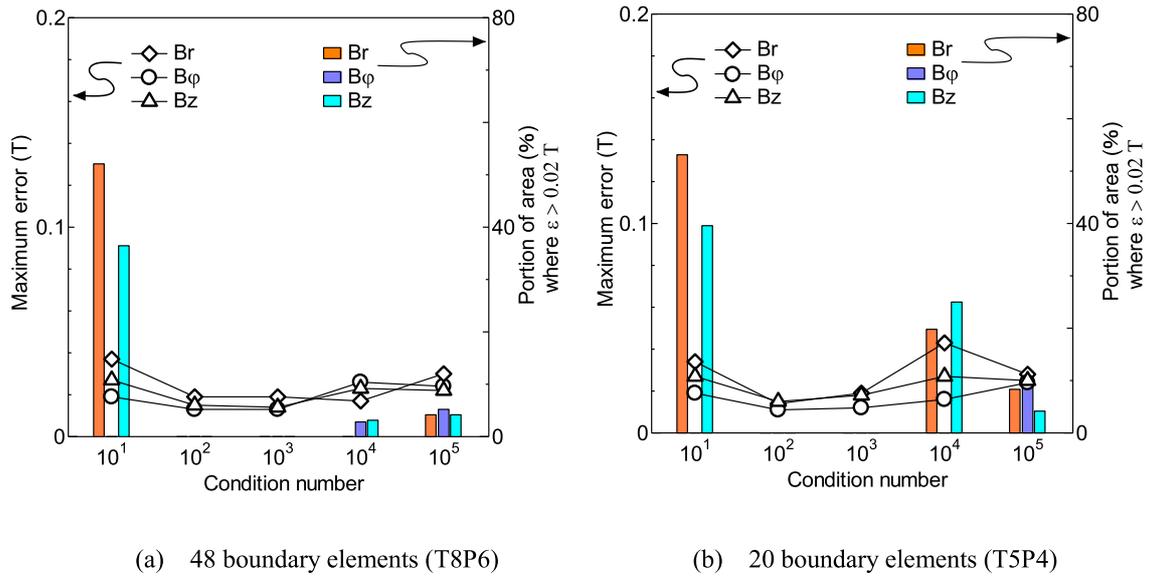
(b) 20 boundary elements (T5P4)

Fig. 6 Error tendency of reconstructed field when assuming 440 field sensors and 126 flux loops. (a) 48 boundary elements (T8P6) (b) 20 boundary elements (T5P4).
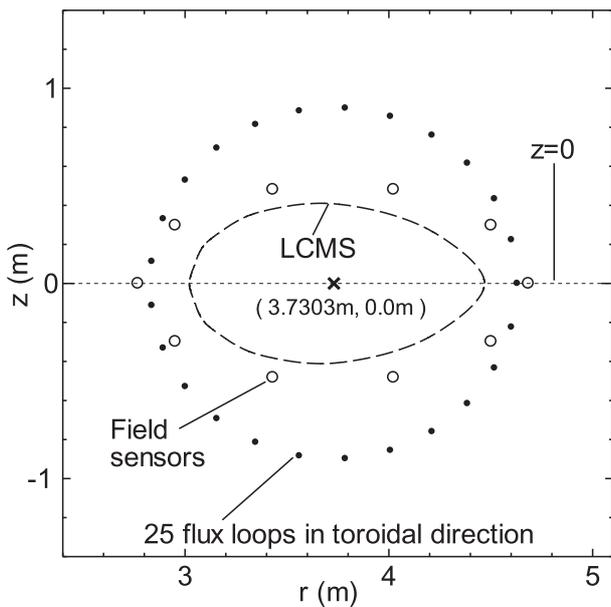

Fig. 7 Sensor locations on the horizontally elongated cross-section: 110 field sensors and 25 flux loops.
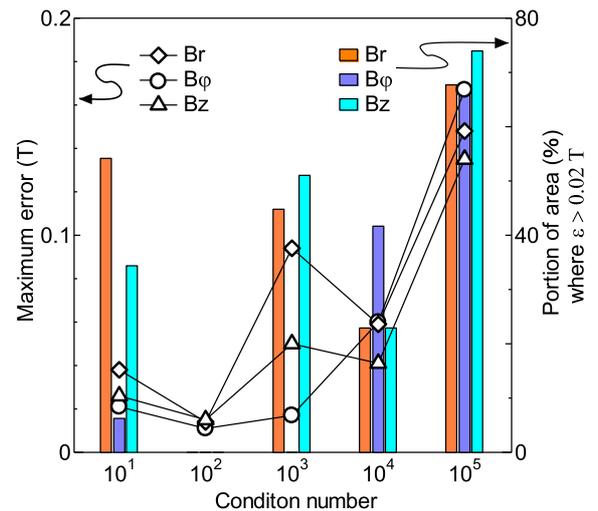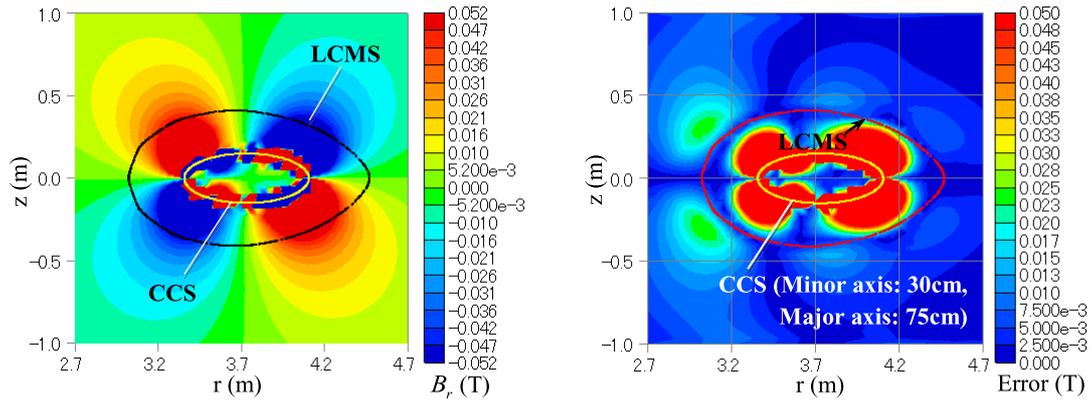

Fig. 8 Error tendency when assuming a smaller number of sensors with 12 boundary elements (T4P3).

the reconstructed solution is shown on the left, while the figure on the right-hand side show the distribution of absolute error, $\varepsilon(\text{T})$, which is calculated as
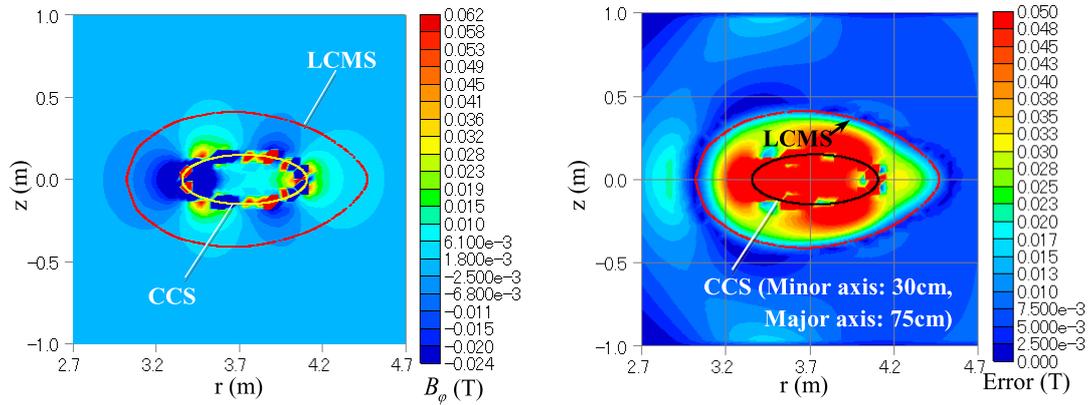
$$\varepsilon(\text{T}) = |\text{Reconstructed value - Reference value}|, \quad (9)$$

respectively for the components of the field, B_r, B_φ and B_z. It can be found that these reconstructed field profiles agree fairly well with the reference ones that are shown on the right in Fig. 4.
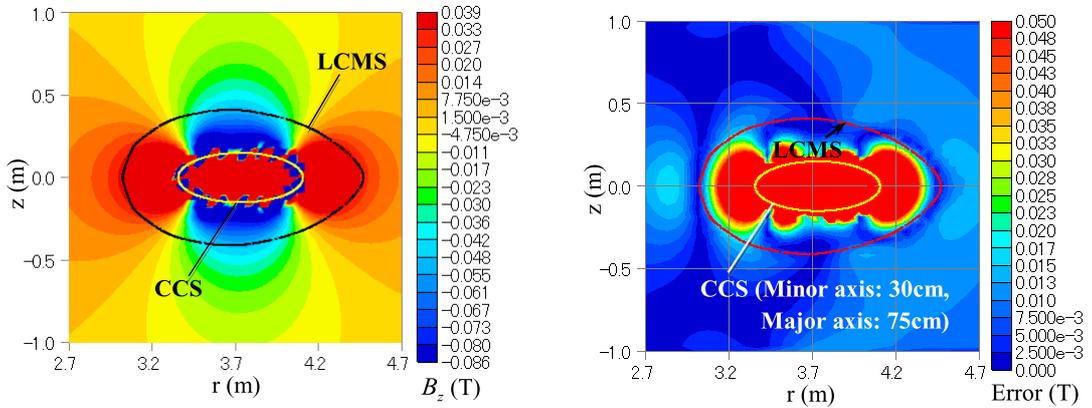
The error tendencies were also investigated for the region $1.0 < \rho < 1.1$ in the minor radius (ρ) space. Table 1 compares the error tendencies between the following two cases:

the drastic reduction in the number of sensors, one will use only 12 boundary elements (T4P3) to enable the analysis.

As shown in Fig. 8, even in this 'economical' case the most accurate field results are obtained when the condition number is set to be 10^2 in such a way that the singular values smaller than the gap threshold are cut off. Figures 9 (a), (b) and (c) depict the field profiles reconstructed under this condition. These figures show the profiles of B_r, B_φ and B_z, respectively on the horizontal elongated cross section when the external coil effect is excluded. In each figure,

(a) B_r (Left: Reconstructed. Right: Absolute error.)

(b) B_φ (Left: Reconstructed. Right: Absolute error.)

(c) B_z (Left: Reconstructed. Right: Absolute error.)

Fig. 9 Reconstructed field caused by plasma current only when assuming a smaller number of sensors with 12 boundary elements (T4P3). (a) B_r (Left: Reconstructed. Right: Absolute error.). (b) B_φ (Left: Reconstructed. Right: Absolute error.). (c) B_z (Left: Reconstructed. Right: Absolute error.).

(i) 12 boundary elements, 110 field sensors and 25 flux loops, the condition number is 10^2,

(ii) 48 boundary elements, 440 field sensors and 126 flux loops, the condition number is 10^5.

The calculation conditions and the results of the latter case are the same as those reported in Ref. [9]. It should be noticed that the accuracy of case (i) results are higher than that of case (ii) in spite of the drastic reduction in the number of sensors.

Table 1   Comparison of the error tendencies.

	(i) 12 boundary elements (110 field sensors & 25 flux loops)			(ii) 48 boundary elements (440 field sensors & 126 flux loops) [9]		
	B_r	B_φ	B_z	B_r	B_φ	B_z
Maximum error(T)	0.020	0.013	0.017	0.030	0.024	0.022
Portion of area where $\varepsilon > 0.02$ T	0.0%	0.0%	0.0%	4.2%	5.2%	4.2%

3.4 Magnetic field line tracing and Poincaré plot

The field caused by the external coils was added to the plasma-current-based field that had been obtained through the CCS analysis. As the coil effect on the magnetic field is ten or more times larger than that of the plasma current effect, the relative errors of B_r, B_φ and B_z in this case are considerably smaller than 5% in the greater part outside the LCMS. A magnetic field line tracing was carried out for the resultant field. This is performed using the MGTRC code [9, 17].

In the same way as the procedure found in Ref. [9], the starting points (r, z, φ) of the traces were set as

$$r = 4.30 + 0.01\,k \text{ in [m] with } k = 0, 1, \cdots, 40, \tag{10}$$

$z = 0.0$ m and $\varphi = 18°$ (the horizontally elongated cross section). Each trace was terminated when the number of toroidal transits reached 100 or when the field line ran out of the analytic domain under consideration.

Figures 10 (a), (b) and (c) show the Poincaré plots on the r-z plane at $\varphi = 18°$ for traces originating at the same starting point $(r, z, \varphi) = (4.47\,\text{m}, 0.0\,\text{m}, 18°)$. Through careful investigation, it was found that this starting point forms the LCMS if the tracing is based on the reference field calculated using the HINT2 code. In each figure, the dashed closed line shows the LCMS for the vacuum field, i.e., $\langle\beta\rangle = 0\%$. This is shifted outward when $\langle\beta\rangle$ takes the nonzero value $\langle\beta\rangle = 2.7\%$. The reference LCMS in this case is the solid closed line. The red round symbols in each figure show the results based on the reconstructed field. The symbols in Figs. 10 (a) and 10 (b) are for the axisymmetric CCS [8] and for the twisted CCS [9] respectively, and both were based on 440 field sensors and 126 flux loops with 48 boundary elements for the CCS. The results in Fig. 10 (c) were also obtained using the twisted CCS but one assumed only 110 field sensors and 25 flux loops with 12 boundary elements, setting the condition number to be 10^2. It is found that in spite of such a small number of sensors being used the scatter of the plot points in Fig. 10 (c) is the narrowest, i.e., the best results among the three cases.
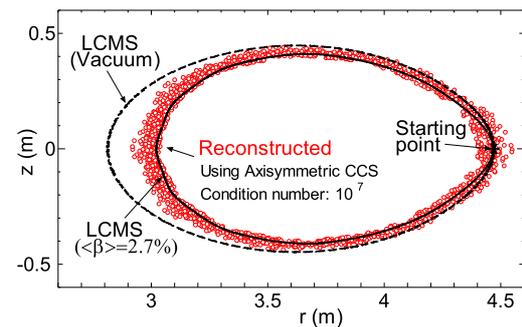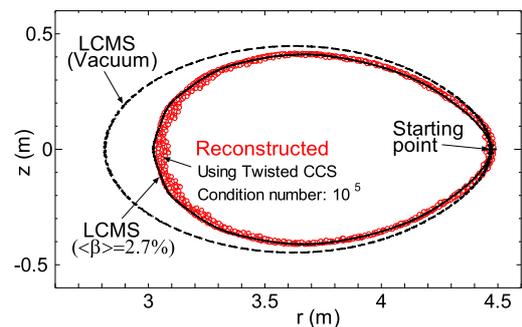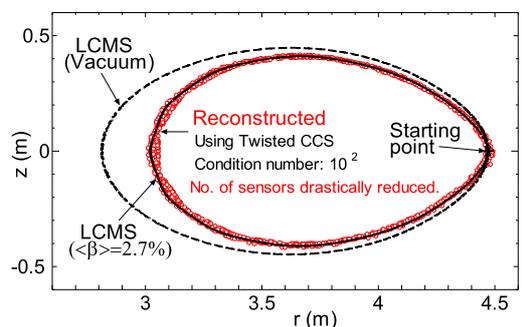

(a) Using the axisymmetric CCS (Cond. No.: 10^7)

(b) Using the twisted CCS (Cond. No.: 10^5)

(c) Using the twisted CCS (Cond. No.: 10^2)

Fig. 10   Poincaré plots for traces originating at $r_{\text{start}} = 4.47$ m. (a) Using the axisymmetric CCS (Cond. No.: 10^7). (b) Using the twisted CCS (Cond. No.: 10^5). (c) Using the twisted CCS (Cond. No.: 10^2).
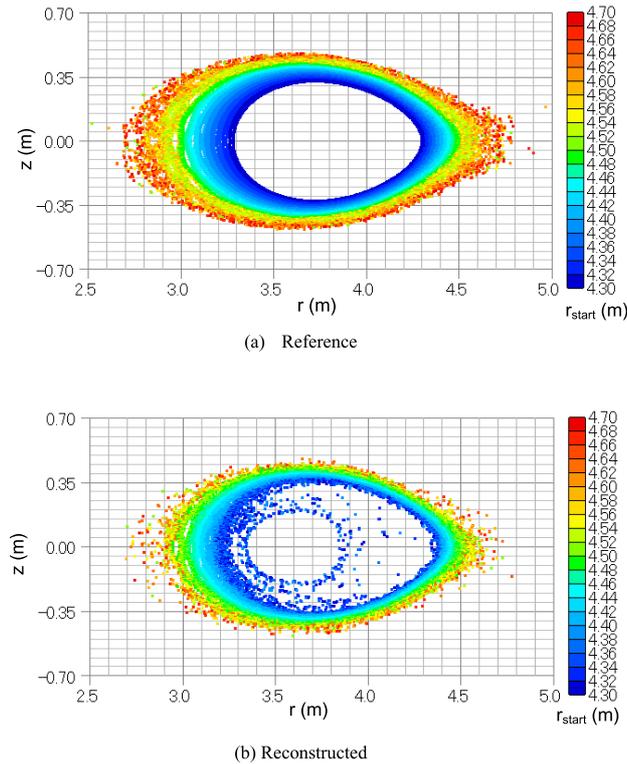
(a) Reference

(b) Reconstructed

Fig. 11   Comparison of Poincaré plots for the reference and the reconstructed field. (a) Reference. (b) Reconstructed.

3.5   Reconstruction of magnetic surfaces

In this section, the discussion is limited to the case assuming 110 field sensors and 25 flux loops with 12 boundary elements (T4P3). Figures 11 (a) and 11 (b) are the Poincaré plots of the field line on the horizontally elongated cross section. Figure 11 (a) is given from the reference field, while Fig. 11 (b) is the result reconstructed under the above calculation conditions.

3.5.1   Poincaré plot for each starting point of the trace

Figures 12 (a)-(d) highlight Poincaré plots for traces originating at different starting points. From these plots the magnetic surface structure may be estimated. In each figure, the red points are the plot for the reconstructed field, while the black points are for the reference field. As the starting point r_{start} = 4.41 m is deep within the plasma region, the reconstructed plot points in Fig. 12 (a) scatter towards the inside of the magnetic surface given by the reference field solution. This is caused by the dirtiness of the CCS method solution under the vacuum field assumption for the plasma region. Although r_{start} = 4.43 m is a little inside the LCMS, the reconstructed plot points in Fig. 12 (b) show passable agreement with the reference ones for the most part. Since r_{start} = 4.52 m is far away from the LCMS, a magnetic surface cannot be recognized in both the reconstructed and the reference Poincaré plots in Fig. 12 (d). The tendency of the scatter of plot points in this figure is almost

the same between the reconstructed and the reference solutions. Figure 12 (c) is a reproduction of Fig. 10 (c). In this figure, the reconstructed Poincaré plot shows a fairly good agreement with the reference one, which is supposed to be the LCMS. However, the plot points are a little scattered and do not always form a closed surface sharply.

3.5.2   quasi magnetic surface

To assist in the magnetic surface estimation, the Poincaré plot points were converted to the 'quasi magnetic surface'. Outline of the technique for this conversion is as follows. Ideally, the r-coordinate of the starting point defined by Eq. (10) can be recognized as a label that corresponds to each magnetic surface if it is a true surface. That is, $r_{start}^{(k)} = \psi(r_{start}^{(k)}, z_{start}^{(k)})$ with

$$z_{start}^{(k)} = 0 \text{ and } r_{start}^{(k)} = 4.30 + 0.01\,k \text{ in [m] with}$$

$$k = 0, 1, \cdots, K. \tag{11}$$

With this idea, the set of discrete Poincaré plot points can be converted to a contour map as a function of $r_{start}^{(k)}$. One here introduces the radial basis function (RBF) expansion [12, 18]

$$\psi(r, z) = \sum_{i=1}^{N} w_i f_i(r, z; r_i, z_i), \tag{12}$$

with N being the number of RBFs and (r_i, z_i) the center of each RBF. In the present work one adopted the thin-plate spline type RBF

$$f_i(r, z; r_i, z_i) = \left\{ \left((r - r_i)^2 + (z - z_i)^2 \right) \middle/ \sigma^2 \right\}$$
$$\log \sqrt{ \left((r - r_i)^2 + (z - z_i)^2 \right) \middle/ \sigma^2}, \tag{13}$$

with the scaling factor σ (=1.0 m). The centers of 100 RBFs were distributed equidistantly in the rectangle domain : (2.2 m < r < 5.2 m, −1.5 m < z < 1.5 m). The unknown weights w_i are determined in a least square manner. The details of the above technique are described in Ref. [9].

The reconstructed Poincaré plot given by Fig. 11 (b) was converted into contours of the quasi magnetic surface that is shown in Fig. 13. Contours are found even outside the LCMS and also deep inside the LCMS, however, they are meaningless and just the result of interpolation in the RBF expansion. As for the latter case the Poincaré plot points originating at r_{start} < 4.30 m were not adopted as sampling points for the expansion.

3.5.3   numerical determination of the LCMS

Itagaki *et al.* [9] proposed a numerical technique to extract the surface that can be regarded as the LCMS from the quasi magnetic surfaces. They introduced the 'scatter' given by
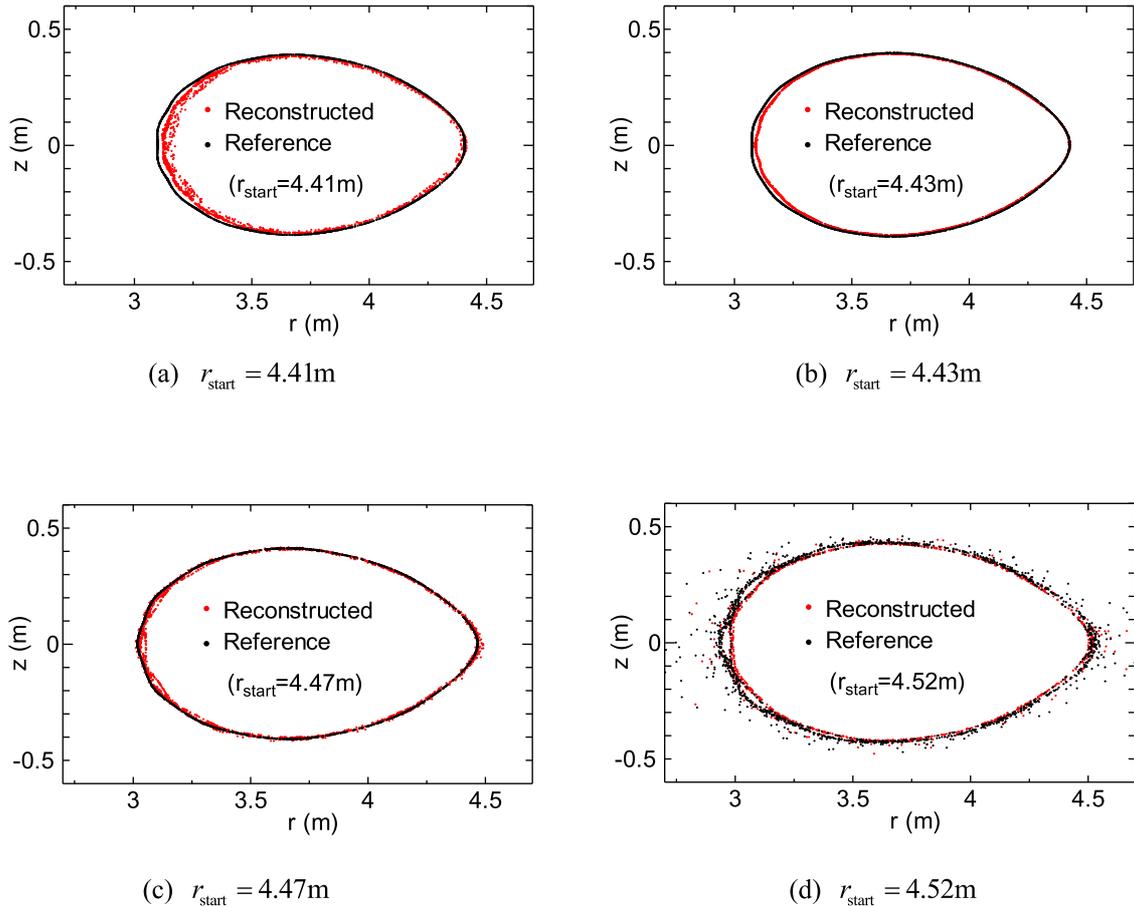
$$s^2 = \frac{1}{m} \sum_{j=1}^{m} d_j^2, \tag{14}$$

(a) $r_{start} = 4.41$m

(b) $r_{start} = 4.43$m

(c) $r_{start} = 4.47$m

(d) $r_{start} = 4.52$m

Fig. 12   Poincaré plots for traces originating at various starting points. (a) r_{start} = 4.41 m. (b) r_{start} = 4.43 m. (c) r_{start} = 4.47 m. (d) r_{start} = 4.52 m.

where d_j denotes the distance between a reconstructed quasi magnetic surface and the j-th point in the m Poincaré plot points corresponding to the surface. Next, they defined the 'inside/outside' ratio (I/O ratio) as

$$R_k = \left(s^2_{inside} / s^2_{outside} \right)_k ,$$ (15)

with s^2_{inside} and $s^2_{outside}$ being the scatters calculated using Eq. (14) respectively for the points inside and outside of the k-th reconstructed surface under consideration. A strong current exists inside the LCMS so that the reconstructed magnetic field profile is very dirty due to the hypothetical vacuum field assumption in the CCS method analysis. Because of this, the ratio tends to take a value larger than unity ($R_k > 1$) inside the LCMS. It was observed in the previous work (see Fig. 15 in Ref. [9]) that the ratio jumps where $r^{(k)}_{start}$ is reduced to a value smaller than 4.47 m, which corresponds to the most probable location of the LCMS.

This technique is also applied to the presently reconstructed quasi magnetic surfaces that are depicted in Fig. 13. The black dashed line in Fig. 14 shows the variation in the I/O ratio as a function of $r^{(k)}_{start}$. The ratio does not readily exceed unity even where $r^{(k)}_{start}$ goes a little inside the LCMS (toward the left in Fig. 14). It increases with the

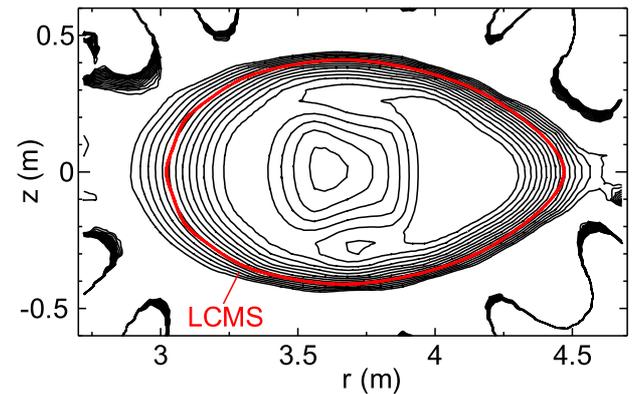Fig. 13   Contours of quasi magnetic surface.

decrease in $r^{(k)}_{start}$ in the region where $r^{(k)}_{start}$ < 4.46 m, but no clear jump indicating the LCMS can be found. This is because the reconstructed field profile at present is substantially accurate even a little inside the LCMS (see Fig. 9). The I/O ratio defined by Eq. (15) should then be modified.

One here notices the 'total scatter', $\tilde{s}^2_k$, which is also calculated using Eq. (14) but for all Poincaré plot points (the points both inside and outside of the quasi surface)
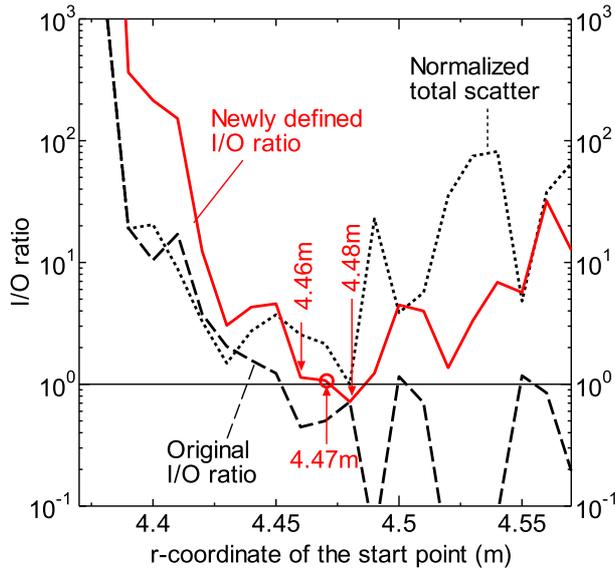
Fig. 14　Variation in the 'inside/outside' ratio

originating at the k-th starting point. Considering the physical assumption in the CCS method, it is understandable that the total scatter tends to take a small value in the vicinity of the LCMS. The black dotted line in Fig. 14 shows the change in the normalized total scatter that is given by

$$\gamma_k = \frac{\tilde{s}_k^2}{\tilde{s}_{\min.}^2}, \tag{16}$$

with $\tilde{s}_{\min.}^2$ being the minimum among the total scatters under consideration. A newly defined I/O ratio is given by

$$\tilde{R}_k = R_k \cdot \gamma_k = \left(\frac{s_{\text{inside}}^2}{s_{\text{outside}}^2}\right)_k \cdot \frac{\tilde{s}_k^2}{\tilde{s}_{\min.}^2}. \tag{17}$$

The red solid line in Fig. 14 shows the variation in $\tilde{R}_k$. The minimum value of this new ratio is at $r_{\text{start}}^{(k)} = 4.48$ m, and the ratio begins to increase significantly when $r_{\text{start}}^{(k)}$ is reduced to 4.46 m. Halfway between the two lies the point for $r_{\text{start}}^{(k)} = 4.47$ m, which corresponds to the correct LCMS given for the reference field.

　　As shown in Fig. 15, one here extracts the quasi magnetic surfaces for $r_{\text{start}}^{(k)} = 4.46$ m, 4.47 m and 4.48 m. Each of them agrees fairly well with the red solid line, i.e., the reference LCMS. It is difficult to judge which value of $r_{\text{start}}^{(k)}$ is the most probable; however, the authors believe that the level of uncertainty observed in Fig. 15 is acceptable at least for operating purposes. It should be stressed that this result was carried out only using the small number of sensors: 110 field sensors and 25 flux loops.

3.6　Consideration of symmetric properties of the field profile

　　When setting the origin of the toroidal angle φ at the horizontally elongated cross section in the LHD, there is
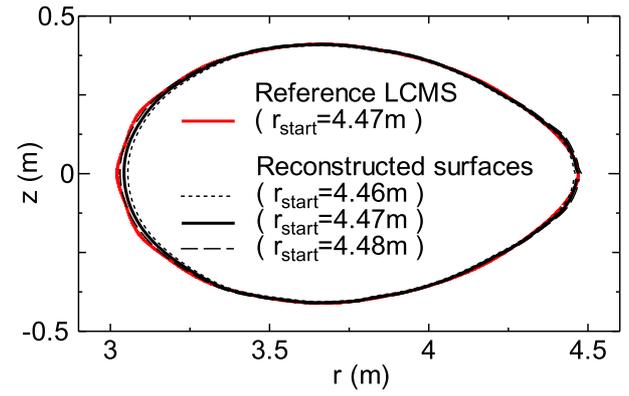

Fig. 15　Reconstructed magnetic surfaces compared with the reference LCMS

the stellarator-symmetry

$$B_r(r, z, -\varphi) = -B_r(r, -z, \varphi), \tag{18a}$$

$$B_z(r, z, -\varphi) = B_z(r, -z, \varphi), \tag{18b}$$

and

$$B_\varphi(r, z, -\varphi) = B_\varphi(r, -z, \varphi). \tag{18c}$$

Also, up-down symmetry exists as follows:

$$B_r(r, z, \varphi_0) = -B_r(r, -z, \varphi_0), \tag{19a}$$

$$B_z(r, z, \varphi_0) = B_z(r, -z, \varphi_0), \tag{19b}$$

and

$$B_\varphi(r, z, \varphi_0) = B_\varphi(r, -z, \varphi_0), \tag{19c}$$

if the toroidal angle φ_0 corresponds to the horizontally or vertically elongated cross section.

　　In the 'economical' analysis, the total of 110 field sensors were placed on 11 different r-z planes with the range of toroidal angle $0° \leq \varphi \leq 36°$, i.e., 10 field sensors on each plane. The horizontally elongated plane $\varphi = 18°$ is the stellarator-symmetry surface. The vertically elongated planes $\varphi = 0°$ and $\varphi = 36°$ are the same as each other due to the periodicity, however, the authors arranged the sensor positions in such a way that no equal positions exist on the planes $\varphi = 0°$ and $\varphi = 36°$ to avoid the singularity of the solution matrix (see Fig. 16).

　　Except for these three planes $\varphi = 0°, 18°$ and $36°$, one can apply the stellarator-symmetry to the sensors. That is, the 40 sensors on 4 planes can be omitted, so the required number of field sensors can be reduced from 110 to 70.

　　In each of the planes $\varphi = 0°, 18°$ and $36°$, 2 out of 10 field sensors are located at $z = 0$, but the other 4 pairs of sensors are symmetrical with respect to the line $z = 0$. Because of this, applying the up-down symmetry, the above 70 sensors can be further reduced to 58 (= $70 - 4 \times 3$).

　　Also, for the signals of flux loops set in the toroidal direction, one finds the up-down symmetry:
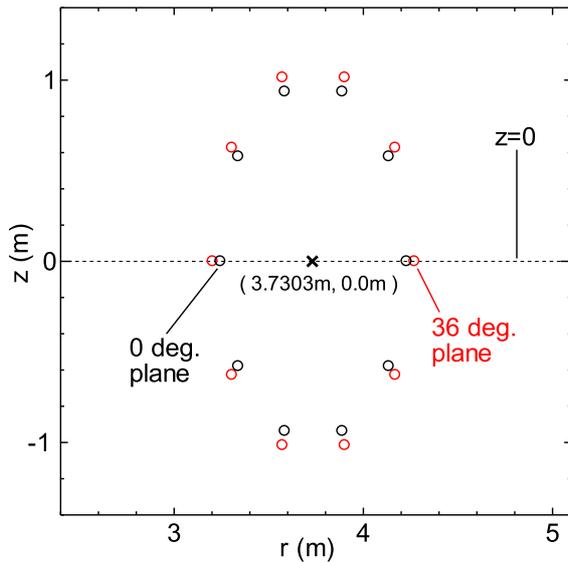
$$\psi^{(Tor)}(r, z) = \psi^{(Tor)}(r, -z). \tag{20}$$

Fig. 16   Field sensor locations on the planes $\varphi = 0°$ and $\varphi = 36°$.

One of the 25 flux loops was set at the position $(r, z) = (4.6303\,\text{m},\ 0.0\,\text{m})$ but the others were set to make 12 pairs each of which has the r-coordinate in common, i.e., (r_k, z_k) and $(r_k, -z_k)$ with $k = 1, 2, \cdots, 12$. Therefore the above number of flux loops, 25, can be reduced to 13.

4. Conclusion

In the reconstruction of the 3D magnetic field profile in the Large Helical Device (LHD), accurate results have been obtained even using only 110 field sensors and 25 flux loops with 12 boundary elements on the CCS when one cuts off the singular values smaller than the gap threshold. The numbers of field sensors and flux loops can be further reduced to 58 and 13 respectively if the symmetry of the field profile in the LHD is considered. This required number is almost the same as the number of magnetic sensors installed in the LHD, so that the present research results suggest the possibility of actual application to the LHD.

Acknowledgments

[1] L.L. Lao, H. St. John, R.D. Stambaugh and W. Pfeiffer, Nucl. Fusion **25**, 1421 (1985).
[2] D.W. Swain and G.H. Neilson, Nucl. Fusion **22**, 1015 (1982).
[3] J. Svensson, A. Werner and JET-EFDA Contributors, Plasma Phys. Control. Fusion **50**, 085002 (2008).
[4] W. Feneberg, K. Lackner and P. Martin, Comp. Phys. Commun. **31**, 143 (1984).
[5] F. Hofmann and G. Tonetti, Nucl. Fusion **28**, 519 (1988).
[6] K. Kurihara, Fusion Eng. Des. **51-52**, 1049 (2000).
[7] M. Itagaki, S. Yamaguchi and T. Fukunaga, Nucl. Fusion **45**, 153 (2005).
[8] M. Itagaki, T. Maeda, T. Ishimaru, G. Okubo, K. Watanabe, R. Seki and Y. Suzuki, Plasma Phys. Control. Fusion **53**, 105007 (2011).
[9] M. Itagaki, G. Okubo, M. Akazawa, Y. Matsumoto, K. Watanabe, R. Seki and Y. Suzuki, Plasma Phys. Control. Fusion **54**, 125003 (2012).
[10] M. Itagaki, T. Ishimaru and K. Watanabe, Proc. the 32nd International Conf. on Boundary Elements and Other Mesh Reduction Methods (Southampton, U.K., 2010), (WIT Press, Southampton, U.K., 2010) p.133.
[11] P.C. Hansen, *Rank-Deficient and Discrete Ill-Posed Problems – Numerical Aspects of Linear Inversion* (Philadelphia: SIAM, 1998).
[12] M.D. Buhmann, *Radial Basis Function* (Cambridge, Cambridge University Press, 2003).
[13] M. Itagaki and N. Sahashi, J. Nucl. Sci. Technol. **33**, 7 (1996).
[14] W.H. Press, B.P. Flannery, S.A. Teukolsky and W.T. Vetterling, *Numerical Recipes - The Art of Scientific Computing* (Cambridge, Cambridge University Press, 1986).
[15] R. Seki, Y. Matsumoto, Y. Suzuki, K. Watanabe and M. Itagaki, Plasma Fusion Res. **3**, 016 (2008).
[16] Y. Suzuki, N. Nakajima, K. Watanabe, Y. Nakamura and T. Hayashi, Nucl. Fusion **46**, L19 (2006).
[17] LHD Experimental Board, LHD Experiment Technical Guide 2009 (Toki, Japan, National Institute for Fusion Science, 2009) Section 6.
[18] M. Itagaki, K. Nakata, H. Tanaka and A. Wakasa, Eng. Anal. Bound. Elem. **33**, 1258 (2009).